Journal of Modern Optics

ISSN: 0950-0340 (Print) 1362-3044 (Online) Journal homepage: http://www.tandfonline.com/loi/tmop20

Attosecond pulse generation isolated with an asymmetric polarization gating

Gao Chen, Eric Cunningham & Zenghu Chang

To cite this article: Gao Chen, Eric Cunningham & Zenghu Chang (2017) Attosecond pulse generation isolated with an asymmetric polarization gating, Journal of Modern Optics, 64:10-11, 952-959, DOI: 10.1080/09500340.2017.1290833

To link to this article: http://dx.doi.org/10.1080/09500340.2017.1290833

JOURNAL OF MODERN OPTICS, 2017
VOL. 64, NOS. 10–11, 952–959
https://doi.org/10.1080/09500340.2017.1290833

Taylor & Francis
Taylor & Francis Group

Attosecond pulse generation isolated with an asymmetric polarization gating

Gao Chen[a,b], Eric Cunningham[a], Zenghu Chang[a]

[a]Institute for the Frontier of Attosecond Science and Technology, Department of Physics, and CREOL, the College of Optics & Photonics, University of Central Florida, Orlando, FL, USA; [b]School of Science, Changchun University of Science and Technology, Changchun, China

ABSTRACT

High harmonics generated using the polarization gating technique are simulated under the strong-field approximation for the cases of equal and unequal ratios between the amplitudes of the two counter-rotating pulses. The effect of the field asymmetry is observed on the high harmonic yield and cut-off in the frequency domain and on the attosecond pulse duration and satellite peak contrast in the time domain. The case where the strong pulse comes later is more favourable in terms of generating a higher cut-off and a shorter pulse duration. It is predicted that thin metal filters can reduce the impact of satellite pulses while simultaneously reducing the pulse duration.

ARTICLE HISTORY
Received 15 September 2016
Accepted 27 January 2017

KEYWORDS
High harmonic generation; isolated attosecond pulse production

1. Introduction

Isolated attosecond pulses are incomparable tools for investigating the electronic behaviour of atoms and molecules (*1*). One way to generate such pulses is a method called polarization gating (PG) (*2–7*): by passing a linearly polarized femtosecond laser pulse through two phase retarders, the polarization of the pulse can be tailored such that the ellipticity varies with time. When driving high harmonic generation (HHG) in a gas target with such a pulse, the production of extreme ultraviolet attosecond bursts can be isolated to a single event if the femtosecond pulse's ellipticity is carefully sculpted to be nearly linear for only one-half of a laser cycle.

Even though the regions of high ellipticity do not contribute to HHG, the laser cycles outside the nearly linear 'polarization gate' nonetheless continue to ionize the gas target. This imposes the primary limitation of the PG technique: for increasing pulse durations or field intensities, leading-edge ionization constrains the number of un-ionized atoms still available for HHG at the time the polarization gate arrives. To avoid this depletion of the gas target, it has been demonstrated previously that a second harmonic field can be added to the PG field ('double optical gating', or DOG) (*8*) and elliptically polarized counter-rotating pulses can be used to form the PG field ('generalized double optical gating', or GDOG) (*9*).

In the cases of PG, DOG and GDOG, the polarization gate is created by overlapping two counter-rotating circularly or elliptically polarized pulses of equal magnitude. Recently, it was proposed that using two counter-rotating pulses of *unequal* magnitude, the arrival time of the polarization gate can be moved forward in time without any change to the width of the polarization gate itself, thus limiting the number of laser cycles on the leading edge of the pulse (*10*). Using the Ammosov–Delone–Krainov (ADK) model (*11*), the ionization rate of these 'asymmetric' gating fields was calculated, the results suggesting a dramatic reduction in ionization compared to the case of typical symmetric gating fields.

As the scope of Ref. (*10*) was limited to the study of leading-edge ionization, these results do not provide insight into the effect of field asymmetry on the spectral and temporal structures of the high harmonic attosecond bursts themselves. To demonstrate the viability of asymmetric fields in forming a sufficiently discriminative polarization gate for isolating individual attosecond pulses, this work compares simulated HHG driven by symmetric and asymmetric gating fields. By choosing simulation parameters in the low-intensity regime to exclude the plasma-induced laser defocusing and phase mismatch, the effect of the field asymmetry itself on the generated high harmonic signal is thereby isolated. This low-intensity regime is also important when phase matching is achieved by balancing plasma effects with neutral gas, which has become a useful phase matching scheme particularly for mid-infrared-driven HHG (*12*). Using the 3D strong-field approximation model and solving the 3D wave propagation equation, the effect of field asymmetry is analysed in terms of its impact on the high-order harmonic cut-off and yield in the frequency domain and on the attosecond pulse duration and contrast in the time domain.

CONTACT Zenghu Chang Zenghu.Chang@ucf.edu

2. Definitions and simulation parameters

To generate a PG field, a linearly polarized pulse passes through two birefringent plates – usually a multi-order full-wave plate followed by a zero-order quarter-wave plate – whose slow and fast axes are oriented at a fixed angle of 45° from each other. The form of this field can be written using the basis defined by the orthogonally polarized driving field $\vec{E}_{drive}$ (responsible for generating high harmonics) and gating field $\vec{E}_{gate}$ (responsible for suppressing high harmonics):

$$\vec{E}_{PG} = \vec{E}_{drive} + \vec{E}_{gate} = E_{drive}\cos(\omega t + \phi_{CE})\hat{e}_1 + E_{gate}\cos\left(\omega t + \frac{\pi}{2} + \phi_{CE}\right)\hat{e}_2 \quad (1)$$

where ω is the carrier frequency and ϕ_{CE} is the carrier envelope phase. The pulse envelopes of the driving and gating fields, E_{drive} and E_{gate} respectively, are given by

$$E_{drive} = \frac{E_0}{\sqrt{2}}\left(\sin\theta_1 \exp\left[-2\ln 2\left(\frac{t+\frac{T_d}{2}}{\tau_p}\right)^2\right] + \cos\theta_1 \exp\left[-2\ln 2\left(\frac{t-\frac{T_d}{2}}{\tau_p}\right)^2\right]\right) \quad (2)$$

$$E_{gate} = \frac{E_0}{\sqrt{2}}\left(\sin\theta_1 \exp\left[-2\ln 2\left(\frac{t+\frac{T_d}{2}}{\tau_p}\right)^2\right] - \cos\theta_1 \exp\left[-2\ln 2\left(\frac{t-\frac{T_d}{2}}{\tau_p}\right)^2\right]\right) \quad (3)$$

where E_0 and τ_p are the electric field amplitude and the pulse duration of the linearly polarized driving laser pulse, respectively, before entering the first birefringent plate and T_d is the separation in time between the two counter-rotating pulses. The angle θ_1 refers to the angle of the polarization direction of the original driving laser pulse compared to the slow axis of the first birefringent plate. The ratio of the magnitudes of the two counter-rotating pulses can be controlled by the angle θ_1 in the following way: when $\theta_1 = \cot^{-1}(1) = 45°$, the incoming pulse is equally projected onto the slow and fast axes of the first birefringent plate, and the magnitudes of the ordinary and extraordinary waves are equal (this is the case of symmetric PG); when the input polarization is rotated such that $\theta_1 \neq 45°$, the pulse is *unequally* projected onto the slow and fast axes of the first birefringent plate, and the magnitudes of the ordinary and extraordinary waves are *not* equal (this is the case of *asymmetric* PG, or APG). In both scenarios, the angle between the slow and fast axes of the first and second birefringent plates remains fixed at 45°, as this condition encapsulates the sharpest possible ellipticity change around the polarization gate. This differs from previous work in which the angle between the two birefringent plates was not held constant, resulting in changes to the HHG spectrum attributable to alterations in the width of the polarization gate itself (*13*, *14*).

When the input polarization projects unequally onto the axes of the first birefringent plate ($\theta_1 \neq 45°$), the point in time at which the envelopes of the two counter-rotating pulses are equal – i.e. the instant of purely linear polarization defining the centre of the polarization gate t_c – changes according to

$$t_c = \frac{\tau_p^2}{T_d}\frac{\ln(\tan\theta_1)}{4\ln 2}. \quad (4)$$

Although the *temporal position* of the polarization gate t_c shifts as a function of the input polarization direction θ_1, the *width* of the polarization gate *remains constant* for all choices of pulse asymmetry because the ellipticity of each counter-rotating pulse is independent of its amplitude. An example of the effect of the input polarization direction θ_1 on the pulse shape and polarization gate is presented in Figure 1.

In the current exercise, near-infrared 800 nm input pulses are simulated using a pulse duration of $\tau_p = 5.33$ fs and a pulse separation of $T_d = 5.33$ fs. The angle θ_1 is varied between the values $\cot^{-1}(2) = 26.6°$, $\cot^{-1}(1) = 45°$ and $\cot^{-1}(1/2) = 63.4°$, corresponding to field ratios of 2:1, 1:1 and 1:2, respectively; these angles are depicted in Figure 2. In order to make a direct comparison of the behaviour of the PG with different field ratios, the envelope of the driving field at the centre of the polarization gate is normalized in each case to $E_{drive}(t_c) = 0.14$ a:u: $= 7.2\times10^8$ V/cm ($\sim 3.4\times10^{14}$ W/cm^2), which is chosen to limit the role of the ionization level of the helium target (< 10% depletion inside the polarization gate for all field ratios). Due to the change in position of the polarization gate with varying θ_1, the carrier envelope phase is also changed according to

$$\phi_{CE} = \frac{\pi}{2} - \omega\frac{\tau_p^2}{T_d}\frac{\ln(\tan\theta_1)}{4\ln 2} \quad (5)$$

to ensure that the positions of the closest two carrier wave extrema straddled the polarization gate in the same way for all three cases. For the 3D wave propagation, the simulation employs a 1 mm-long helium gas cell, which is centred 1.5 mm after the laser focus. The assumed focal spot size is $w_0 = 25$ μm, which corresponds to a Rayleigh range of $z_R = 2.6$ mm. Plasma effects are ignored in this simulation, which is a valid assumption given the low ionization probability; the density of the helium target

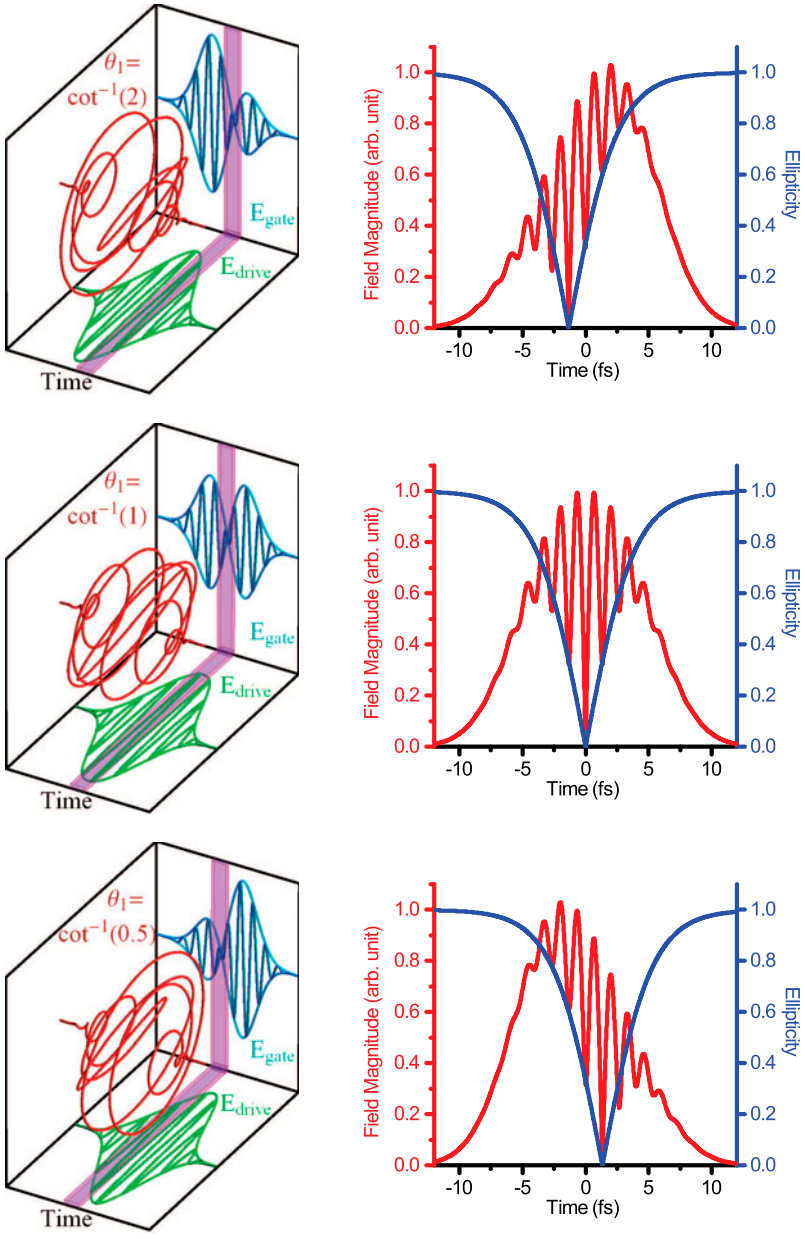

Figure 1. The top, middle and bottom rows show the cases of $\theta_1 = \cot^{-1}(1/2)$, $\cot^{-1}(1)$ and $\cot^{-1}(2)$, respectively. On the left, the total field (red), gating field (blue), driving field (green) and polarization gate (magenta) are plotted as a function of time for all three field ratios. On the right, the absolute field magnitude $||\vec{E}_{PG}||$ (red) and ellipticity (blue) are plotted as a function of time for all three field ratios.

itself is taken to be held at a constant value of $1.3 \times 10^{18}\,\mathrm{cm}^{-3}$.

The high-order harmonic spectrum obtained in a macroscopic medium is determined by two processes: a single-atom response and a three-dimensional non-adiabatic propagation. For this simulation, the harmonic spectrum from a single atom is first calculated using the strong-field approximation model (*15*). Previous work has shown that the intensity of the harmonic spectrum along the y-direction is much lower than that along the x-direction. Thus, the instantaneous dipole moment of an atom in the x-direction is described in atomic units as

$$x(t) \approx i \int_{-\infty}^{t} \mathrm{d}t' \left(\frac{\pi}{\epsilon + i(t-t')/2}\right)^{3/2} \times d_x^*\left[\vec{p}_{st}(t',t) - \vec{A}(t)\right] \exp\left[-iS_{st}(\vec{p}_{st},t',t)\right] \times \vec{d}\left[\vec{p}_{st}(t',t) - \vec{A}(t')\right] \cdot \vec{E}(t')g(t) + C.C. \quad (6)$$

where ϵ is a positive small number, $\vec{E}(t)$ is the electric field of the laser pulse and $\vec{A}(t)$ is its associated vector potential. The ground-state amplitude is given as

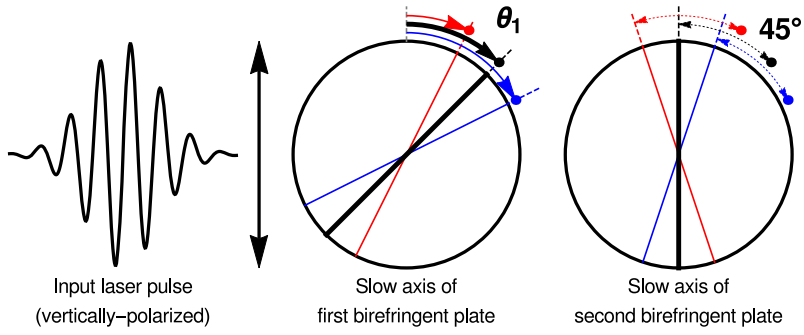

Figure 2. The orientation of the slow axes of the two birefringent plates required to produce APG pulses with field ratios of 2:1 ($\theta_1 = \cot^{-1}(2) = 26.6°$, red), 1:1 ($\theta_1 = \cot^{-1}(1) = 45°$, black) and 1:2 ($\theta_1 = \cot^{-1}(1/2) = 63.4°$, blue). The electric field resulting from such a setup is visible for each choice of θ_1 in Figure 1.

$g(t) = \exp\left(-\int_{-\infty}^{t} w(t'')\mathrm{d}t''\right)$, with the ionization rate $w(t'')$ calculated using the ADK model (*11*). The quasi-classical action of the electron S_{st} is expressed as

$$S_{st}(\vec{p}_{st}, t', t) = (t - t')I_p - \frac{1}{2}p_{st}^2(t', t)(t - t') + \frac{1}{2}\int_{t'}^{t} A^2(t'')\mathrm{d}t''. \quad (7)$$

Here, I_p is the ionization potential of the helium atom chosen as the target gas, and $\vec{p}_{st}$ is the canonical momentum of the electron corresponding to a stationary phase, which can be given by

$$\vec{p}_{st}(t', t) = \frac{1}{t - t'}\int_{t'}^{t} \vec{A}(t'')\mathrm{d}t''. \quad (8)$$

The harmonic spectrum for a single atom is then obtained by Fourier transforming the dipole acceleration $\vec{a}(t) = \ddot{x}(t)$.

Next, the harmonic field propagation in a macroscopic medium is simulated by solving a three-dimensional propagation equation (*16*). In our simulation, because of the low ionization probability and the low density of atoms in the medium, the effects of dispersion, the Kerr non-linearity and plasma defocusing on the fundamental laser field can be neglected. The fundamental laser field is assumed to be a Gaussian beam in space. Its spatial and temporal dependence can be expressed in an analytical form (*16*).

For high harmonics, dispersion and absorption effects from the medium depend linearly on gas pressure and could be ignored under low pressure. The free-electron dispersion is also neglected since the plasma frequency is much smaller than the frequencies of high harmonics. The propagation of harmonic field in the ionizing medium is described by the equation

$$\nabla^2 E_h(r, z, t) - \frac{1}{c^2}\frac{\partial^2 E_h(r, z, t)}{\partial t^2} = \mu_0 \frac{\partial^2 P_{nl}(r, z, t)}{\partial t^2}, \quad (9)$$

where r is the transverse coordinate, z is the propagation coordinate in the lab frame, c is the speed of light in vacuum and μ_0 is the permeability of free space. The non-linear polarization of the medium in the laser pulse is

$$P_{nl}(r, z, t) = \left[n_0 - n_e(r, z, t)\right]x(r, z, t) \quad (10)$$

Here, n_0 is the neutral atom density ($1.3 \times 10^{18}/\mathrm{cm}^3$), and the free-electron density is given by $n_e(r, z, t) = n_0\left[1 - g(t)\right]$. The induced dipole moment $x(r, z, t)$ is calculated with Equation (6) for atoms inside the medium under the influence of the fundamental laser field, which gives the atomic response to the entire laser pulse. When we transform the coordinate from the laboratory frame into the moving frame ($z' = z$ and $t' = t - z/c$) and employ the paraxial approximation, we obtain

$$\nabla_\perp^2 E_h(r, z', t') - \frac{2}{c}\frac{\partial^2 E_h(r, z', t')}{\partial z' \partial t'} = \mu_0 \frac{\partial^2 P_{nl}(r, z', t')}{\partial t'^2}. \quad (11)$$

By adopting the Fourier transform, the temporal derivative in this equation can be eliminated:

$$\nabla_\perp^2 E_h(r, z', \omega) - \frac{2i\omega}{c}\frac{\partial \tilde{E}_h(r, z', \omega)}{\partial z'} = -\mu_0\omega^2 \tilde{P}_{nl}(r, z', \omega), \quad (12)$$

$$\tilde{E}_h(r, z', \omega) = \hat{F}\left[E_h(r, z', t')\right],\ \tilde{P}_{nl}(r, z', \omega) = \hat{F}\left[P_{nl}(r, z', t')\right] \quad (13)$$

where $\vec{F}$ is the Fourier transform operator acting on the temporal coordinate. These equations are solved numerically: Equation (6) is computed for each frequency in a spatial grid with 600 points and 400 points in the r and z directions, respectively, and then the single-atom

dipole moments at the grid points are calculated and entered into Equation 12, which is solved using the Crank–Nicholson method.

Once the harmonic field is obtained at the exit face ($z' = z_{out}$), the HHG spectrum at the macroscopic level can be obtained by integration over the transverse direction (*17*):

$$I_h(\omega) \propto \int_0^\infty \left|\tilde{E}_h(r, z_{out}, \omega)\right|^2 2\pi r \, \mathrm{d}r. \quad (14)$$

The intensity of attosecond pulses can then be calculated as

$$I(t) = \int_0^\infty 2\pi r \, \mathrm{d}r \left| \int_{\omega_1}^{\omega_2} \tilde{E}_h(r, z_{out}, \omega) e^{i\omega t} \mathrm{d}\omega \right|^2. \quad (15)$$

3. Simulation results – frequency domain

The simulated single-atom and macroscopic harmonic signals for the pulse parameters described above are plotted in Figure 3. Even though the pulse envelope at the centre of the polarization gate is normalized, two differences between the three field ratios are immediately apparent: (1) the relative intensity and (2) the harmonic cut-off. Both of these effects can be explained by examining the relative character of the driving field near the polarization gate in all three cases, as displayed in Figure 4. In the case of $\theta_1 = \cot^{-1}(2)$, the leading pulse is small while the trailing pulse is large; therefore, the first field extremum is *smaller* and the second field extremum is *larger* than $E_{drive}(t_c)$. Conversely, in the case of $\theta_1 = \cot^{-1}(1/2)$, the leading pulse is large while the trailing pulse is small; therefore, the first field extremum is *larger* and the second field extremum is *smaller* than $E_{drive}(t_c)$. In the symmetric case of $\theta_1 = \cot^{-1}(1)$, the leading pulse and the trailing pulse are equal in magnitude; therefore, the first field extremum and the second field extremum are both nearly the same as $E_{drive}(t_c)$.

These differences alter the character of the HHG process. In the first stage of the three-step model, the intense field is responsible for electron *ionization*; with all other parameters equal, a stronger *ionization-inducing* field will therefore result in more freed electrons, which will lead to more recombination events and higher harmonic yield. In the second stage of the three-step model, the intense field, now with opposite direction, is responsible for electron *acceleration*; with all other parameters equal, a stronger *accelerating* field will therefore result in higher electron kinetic energies, which will lead to higher harmonic cut-offs. This is why the case of $\theta_1 = \cot^{-1}(1/2)$ features the highest yield and the lowest cut-off, while the case of $\theta_1 = \cot^{-1}(2)$ features the lowest yield and the highest cut-off. It is worthwhile to note

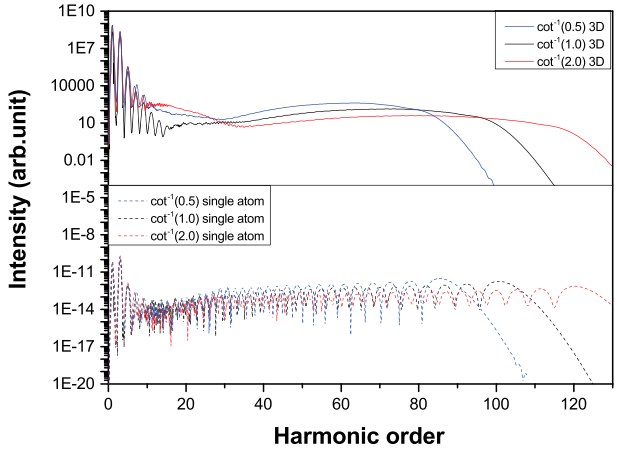

Figure 3. Single-atom (bottom) and 3D macroscopic (top) harmonic spectra generated by PG fields with different field ratios.

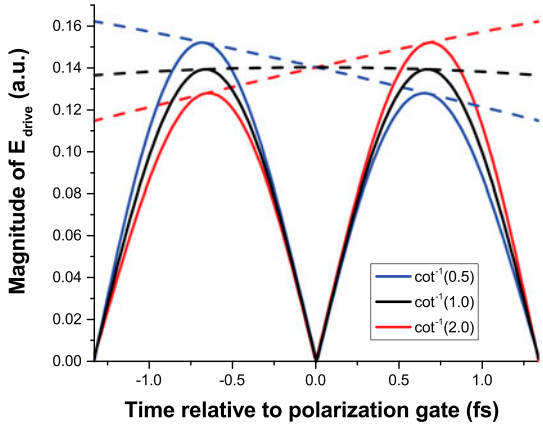

Figure 4. Driving field extrema surrounding the polarization gate for different field ratios. While the envelope of all three fields (dotted lines) are normalized at the centre of the polarization gate, the fields themselves (solid lines) differ in magnitude because of the field asymmetry.

that a similar trade-off has been observed previously in a simulation of high harmonics generated by two-colour driving fields: as the phase difference between the fundamental and second harmonic beams was scanned, the harmonic yield and the harmonic cut-off trended in opposite directions (*18*).

4. Simulation results – time domain

Figure 5 shows the macroscopic spectra from Figure 3 transformed into the time domain using the harmonics of order 20 and higher. Compared to the symmetric case of $\theta_1 = \cot^{-1}(1)$ that yields a pulse duration of 158 as (44 as transform limit), the case of $\theta_1 = \cot^{-1}(1/2)$ expectedly features a higher yield and longer pulse duration (169 as; 56 as transform limit), and the case of $\theta_1 = \cot^{-1}(2)$ unsurprisingly features a lower yield and shorter pulse duration (151 as; 30 as transform limit). The temporal

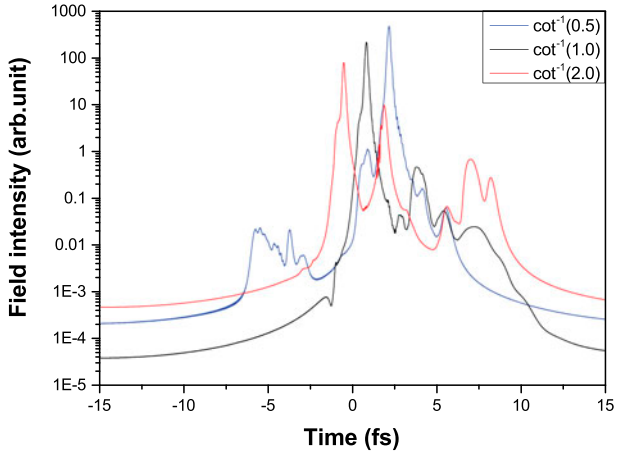

Figure 5. The temporal profile of the isolated attosecond pulses corresponding to the macroscopic HHG spectra plotted in the top panel in Figure 3.

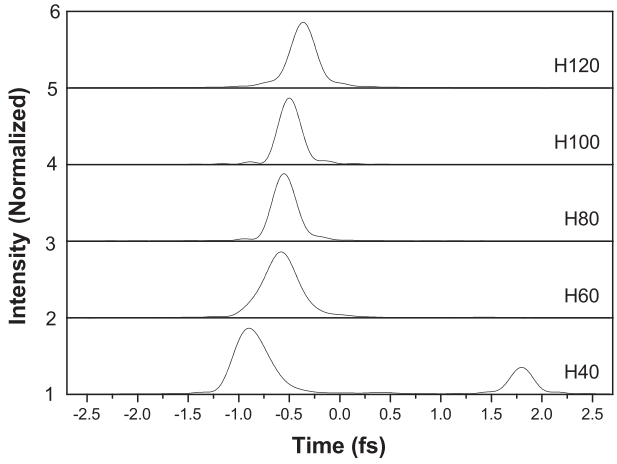

Figure 6. The temporal profile of 20 harmonic-wide ranges of the macroscopic spectrum corresponding to $\theta_1 = \cot^{-1}(2)$ in the top panel of Figure 3 (red curve). Each range is centred at the harmonic order specified at the right of each panel (H40, …, H120). The satellite pulse is only apparent when selecting the lowest order harmonic region.

displacement between the three attosecond pulses merely reflects the difference in the position of the polarization gates in each scenario.

It is important to note that while the amplitude of the main pulse is more than two orders of magnitude larger than the amplitude of the largest satellite pulse for the symmetric case of $\theta_1 = \cot^{-1}(1)$, this ratio is instead closer to 10% for the case of $\theta_1 = \cot^{-1}(2)$. This indicates that even though the width of the polarization gate – and thus the recombination efficiency – remains unchanged, the use of field asymmetry may actually increase the total electron recombination in regions of relatively high ellipticity due to the greater *number* of electrons ionized by the stronger electric fields on the outer edges of the polarization gate.

To understand this effect, it is first noted that there is *not* a reduction in satellite pulse contrast for the case of $\theta_1 = \cot^{-1}(1/2)$. Because the stronger laser cycle arrives *before* the polarization gate, this cycle's short-trajectory electrons remain too far from the low-ellipticity region to allow any significant electron recombination. Even though this cycle's long-trajectory electrons *do* fall close to the early edge of the polarization gate, the photoemission from these electrons is typically suppressed in the macroscopic signal due to phase matching (*19*). As a result, no strong satellite pulse is obvious for the case of $\theta_1 = \cot^{-1}(1/2)$ in Figure 5.

On the other hand, the stronger laser cycle arrives *after* the polarization gate in the case of $\theta_1 = \cot^{-1}(2)$. Now, the recombination of this cycle's short-trajectory electrons occurs close enough to the late edge of the polarization gate that electron recombination is not suppressed as completely. Since photoemission from the short-trajectory electrons typically comprises the macroscopic signal, a comparatively stronger satellite pulse is perceptible for the case of $\theta_1 = \cot^{-1}(2)$ in Figure 5.

To characterize this satellite pulse, Figure 6 plots the temporal profile of 20 harmonic-wide segments of the macroscopic spectrum (from Figure 3) for the case of $\theta_1 = \cot^{-1}(2)$, showing that the satellite pulse is comprised of only the lowest order harmonic photoemission ($t \sim 1.75$ fs in bottom panel). This is because typical recombination events carry an intrinsic atto-chirp (*19*): for short-trajectory electrons, the lowest order harmonics are generated *first* and the cut-off harmonics are generated *last* (as also illustrated by the shift of the main peaks in Figure 6). Referring to the case of $\theta_1 = \cot^{-1}(2)$: because the ellipticity is still rapidly increasing in the region far from the centre of the polarization gate where the satellite pulse is produced, the atto-chirp dictates that the generation of cut-off harmonics in this region is far less efficient than the lowest order harmonics which are generated closer to (albeit still far removed from) the polarization gate.

This analysis suggests that removing the lower energy portion of the harmonic spectrum will improve the contrast ratio between the amplitudes of the primary and satellite attosecond pulses. In a laboratory setting, this filtering can be accomplished using thin metal filters, which are already added to many HHG setups in order to remove the residual energy from the near-infrared driving laser. For this simulation, a zirconium filter was used because of its spectral cut-off near 70 eV, which is close to the 45$^{\text{th}}$ harmonic of the 800 nm driving laser. Using the case of $\theta_1 = \cot^{-1}(2)$, Figure 7 plots the macroscopic spectrum from Figure 3 in gray, the filtered macroscopic spectrum in red and the transmission curve of the zirconium filter in blue.

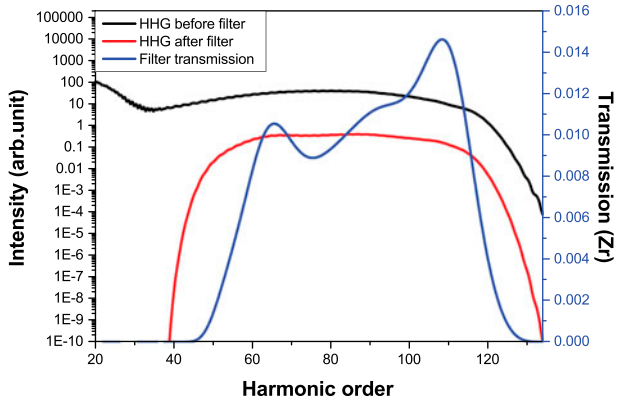

Figure 7. The effect of a 1400-nm-thick zirconium filter on the macroscopic spectrum in the top panel of Figure 3 for the case of $\theta_1 = \cot^{-1}(2)$ (red curve).

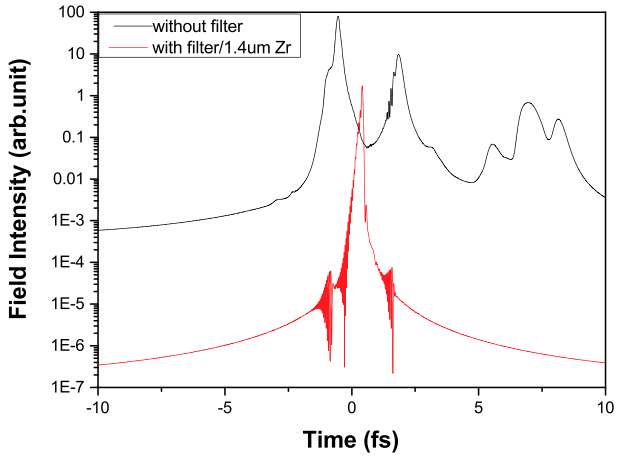

Figure 8. The temporal profiles of the attosecond pulses corresponding to the HHG spectra shown in Figure 7.

The thickness of the zirconium filter was chosen to be 1400 nm. This thickness was specifically chosen to provide an amount of material dispersion that matches the intrinsic phase of the HHG as closely as possible. In this way, the pulse contrast can be improved while simultaneously compressing the attosecond pulse to much shorter temporal durations (*20*). Figure 8 demonstrates the effect of the 1400-nm zirconium filter on the macroscopic spectrum when using $\theta_1 = \cot^{-1}(2)$: the pulse contrast improves by over three orders of magnitude, while the pulse duration is compressed from 151 as to 59 as.

5. Conclusion

Previous work investigating polarization-based gating of attosecond pulses implies that when the field ratio is chosen such that the smaller pulse arrives first, superior ionization suppression allows the high harmonic cut-off to be increased using high intensities; this work furthermore suggests an additional enhancement of the high harmonic cut-off compared to the symmetric case because the field maximum on the trailing edge of the polarization gate is relatively large. While satellite pulse production is also predicted in this case where the larger pulse comes second, this work demonstrates that the satellite pulses are largely comprised of the lowest order high harmonics because only the shortest short-trajectory electrons can emit high harmonics before the quickly increasing ellipticity at the edge of the polarization gate renders the process too inefficient. This allows the satellite pulses to be eliminated through spectral filtering, which is already a part of many common isolated attosecond pulse setups for filtering out residual low-energy photons from the driving laser field. This supports the assertion that asymmetric gating fields provide an experimentally viable option for generating isolated attosecond pulses with higher harmonic cut-offs and shorter pulse durations than otherwise possible with symmetric gating fields. It is expected that this technique may also be used with other gating methods (e.g. DOG and GDOG for using multicycle pulses) or with longer wavelength driving lasers for increasing the high harmonic cut-off even further.

Disclosure statement

No potential conflict of interest was reported by the authors.

Funding

This work has been supported Army Research Office [grant number W911NF-14-1-0383], [grant number W911NF-15-1-0336]; Air Force Office of Scientific Research [grant number FA9550-15-1-0037]; the DARPA PULSE program by a grant from AMRDEC [W31P4Q1310017]; the Jilin Provincial Research Foundationor Basic Research; the National Science Foundation under NSF [grant number 1506345]. Any opinions, findings and conclusions or recommendations expressed in this material are those of the authors and do not necessarily reflect the views of the National Science Foundation.

ORCID

Eric Cunningham http://orcid.org/0000-0002-0976-4416

References

(1) Chini, M.; Zhao, K.; Chang, Z. *Nat. Photon.* **2014,** *8,* 178–186.
(2) Corkum, P.B.; Burnett, N.H.; Ivanov, M.Y. *Opt. Lett.* **1994,** *22,* 1870–1872.
(3) Ivanov, M.; Corkum, P.B.; Zuo, T.; Bandrauk, A. *Phys. Rev. Lett.* **1995,** *74,* 2933–2936.

(4) Platonenko, V.T.; Strelkov, V.V.J. *Opt. Soc. Amer. B* **1999,** *16,* 435–440.
(5) Chang, Z. *Phys. Rev. A* **2004,** *70,* 043802.
(6) Sola, I.J.; Mével, E.; Elouga, L.; Constant, E.; Strelkov, V.; Poletto, L.; Villoresi, P.; Benedetti, E.; Caumes, J.-P.; Stagira, S.; Vozzi, C.; Sansone, G.; Nisoli, M. *Nat. Phys.* **2006,** *2,* 319–322.
(7) Tcherbakoff, O.; Mével, E.; Descamps, D.; Plumridge, J.; Constant, E. *Phys. Rev. A* **2003,** *68,* 043804.
(8) Mashiko, H.; Gilbertson, S.; Li, C.; Khan, S.D.; Shakya, M.M.; Moon, E.; Chang, Z. *Phys. Rev. Lett.* **2008,** *100,* 103906-1–103906-4.
(9) Feng, X.; Gilbertson, S.; Mashiko, H.; Wang, H.; Khan, S.D.; Chini, M.; Wu, Y.; Zhao, K.; Chang, Z. *Phys. Rev. Lett.* **2009,** *103,* 183901-1–183901-4.
(10) Cunningham, E.; Chang, Z. *IEEE J. Sel. Top. Quantum Electron.* **2015,** *21,* 1–6.
(11) Ammosov, M.V.; Delone, N.B.; Krainov, V.P. *Sov. Phys. JETP* **1986,** *64,* 1191–1194.
(12) Takahashi, E.J.; Kanai, T.; Ishikawa, K.L.; Nabekawa, Y.; Midorikawa, K. *Phys. Rev. Lett.* **2008,** *101,* 253901-1–253901-4.
(13) Strelkov, V.; Zair, A.; Tcherbakoff, O.; López-Martens, R.; Cormier, E.; Mével, E.; Constant, E. *Appl. Phys. B* **2004,** *78,* 879–884.
(14) Kolliopoulos, G.; Carpeggiani, P.A.; Rompotis, D.; Charalambidis, D.; Tzallas, P. *Rev. Sci. Instrum.* **2012,** *83,* 063102.
(15) Lewenstein, M.; Balcou, Ph; Ivanov, MYu; L'Huillier, A.; Corkum, P.B. *Phys. Rev. A* **1994,** *49,* 2117–2132.
(16) Jin, C.; Le, A.T.; Lin, C.D. *Phys. Rev. A* **2009,** *79,* 053413.
(17) Li, P.C.; Chu, S.I. *Phys. Rev. A* **2012,** *86,* 013411.
(18) Mauritsson, J.; Johnsson, P.; Gustafsson, E.; L'Huillier, A.; Schafer, K.J.; Gaarde, M.B. *Phys. Rev. Lett.* **2006,** *97,* 013001.
(19) Chang, Z. *Phys. Rev. A* **2005,** *71,* 023813.
(20) Kim, K.T.; Kim, C.M.; Baik, M.-G.; Umesh, G.; Nam, C.H. *Phys. Rev. A* **2004,** *69,* 051805.